

XMM-Newton observations of two X-ray bright galaxy groups – pushing out to r_{500}

J. Rasmussen^{1*} and T. J. Ponman²

¹ *Astronomical Observatory, University of Copenhagen, Juliane Maries Vej 30, DK-2100 Copenhagen Ø, Denmark*

² *School of Physics and Astronomy, University of Birmingham, Edgbaston, Birmingham B15 2TT, UK*

ABSTRACT

We report on the results of *XMM-Newton* observations of the $z = 0.18$ galaxy group WARPJ0943.7+1644 and the nearby poor cluster WARPJ0943.5+1640 at $z = 0.256$. Tracing the X-ray gas out to $\sim 425h^{-1}$ and $\sim 500h^{-1}$ kpc in the two systems, corresponding to roughly 70 per cent of the estimated virial radii, we find the surface brightness profile of both groups to be well described by standard β -models across the entire radial range, but with a significantly lower value of β in the cooler WARPJ0943.7+1644. A Navarro-Frenk-White (NFW) model for the gas density can also provide a good fit to the surface brightness data, but a large scale radius is required, and gas-traces-mass is strongly ruled out. Both systems fall close to the observed $L_X - T$ relation for clusters. Gas mass fractions increase with radius out to the radii probed, reaching extrapolated values at the virial radius of 0.08 and $0.09h^{-3/2}$, respectively. The latter is concordant with results obtained for more massive systems. Gas entropy profiles show evidence for excess entropy out to at least r_{500} , and are inconsistent with predictions of simple preheating models. This study emphasizes the need for observing galaxy groups out to large radii, to securely establish their global properties.

Key words: galaxies: clusters: individual: WARPJ0943.7+1644 – galaxies: clusters: individual: WARPJ0943.5+1640 – cosmology: observations – X-rays: galaxies: clusters.

1 INTRODUCTION

Groups of galaxies are of fundamental importance to our understanding of the mass distribution in the Universe. The majority of galaxies are found in groups (Tully 1987), and the hot intergalactic gas in groups appears likely to represent the dominant component of the Universal baryon content (Fukugita, Hogan & Peebles 1998). However, observation of this gas presents a problem. The small size of groups, compared to rich clusters, results in lower X-ray surface brightness, with the result that whilst cluster gas in some rich systems has been mapped out to approximately the virial radius r_{200} , defined here as the radius containing a mean overdensity of 200 with respect to the critical density, the emission from galaxy groups is typically lost in the X-ray background at $r \lesssim r_{200}/3$.

The seriousness of the problem is aggravated by the fact that surface brightness profiles in poor systems are usually much *flatter* than those in clusters (Ponman, Cannon & Navarro 1999; Sanderson et al. 2003), probably due to the action of non-gravitational processes such as galaxy winds.

Adopting the popular β -model parametrization for the X-ray surface brightness S ,

$$S(r) = S_0[1 + (r/r_c)^2]^{-3\beta+1/2}, \quad (1)$$

galaxy groups are generally found to have $\beta \lesssim 0.5$ (Helsdon & Ponman 2000), in comparison to $\beta \approx 0.67$ in clusters (e.g. Jones & Forman 1984; Mohr et al. 1995). Hence both the luminosity and gas mass formally diverge at large radius in groups.

The low X-ray surface brightness of galaxy groups has so far precluded the detection of the hot gas at large radii which should dominate their baryon content. It is important to derive observational constraints on the properties of this gas to larger radii, for a number of reasons. One can find many examples in the literature of authors concluding that galaxy groups have low gas mass fractions (defined as the ratio of gas mass to total mass), on the basis of an X-ray analysis extending to only $r \sim 200$ kpc. While it is known that galaxy groups contain large amounts of dark matter, it is not yet clear whether their mass-to-light ratios and total baryon fractions are indistinguishable from those of clusters, since they have not been measured to large radii. Given the dominant contribution of groups to the mass function of virialised systems, this has a substantial impact on attempts to eval-

* E-mail: jr@astro.ku.dk

uate the observed mass and baryon content of the Universe. It is not clear how properties measured within $\sim r_{200}/3$ should be extrapolated to r_{200} to obtain integrated values for whole systems and provide ‘templates’ for the interpretation of other poor systems. For example, it is not obviously appropriate to fit a β -model and use this to extrapolate the X-ray luminosity or gas density distribution. The unphysical divergence at large radius discussed above, implies that such a profile *must* turn over at some radius, and one needs to know where. In addition, the β -profile has little theoretical justification and better descriptions might be at hand. For example, Navarro, Frenk & White (1995; NFW hereafter) find from cosmological simulations that out to r_{200} , profiles of both dark matter and gas density in clusters are better fitted by a model of the form

$$\rho(r) \propto \frac{1}{(r/r_s)(1 + r/r_s)^2} \quad (2)$$

(see also Moore et al. 1998). Here r_s is a characteristic scale radius related to the mass of the system. However, these simulations do not allow for extra physics, such as galaxy winds and radiative cooling, which may radically alter the gas profiles, especially in low-mass systems. There is no substitute for actually observing how the gas behaves at large radii.

With the arrival of *XMM-Newton*, we have the opportunity for the first time to measure the X-ray properties of galaxy groups to large radius. Here we report on the results of *XMM-Newton* observations of the galaxy groups WARPJ0943.7+1644 (hereafter referred to in the text as WJ943.7) and WARPJ0943.5+1640 (hereafter WJ943.5 in the text), aimed at mapping and characterizing the X-ray gas out to a considerable fraction of r_{200} . These X-ray sources are close on the sky and were targeted in a single *XMM* pointing; they were both detected serendipitously in a 9 ks *ROSAT* PSPC pointing as part of the WARPS X-ray cluster survey (Scharf et al. 1997; Jones et al. 1998). The extended X-ray emission of the systems was also confirmed by their subsequent detection in the CfA 160 deg² survey (Vikhlinin et al. 1998; Mullis et al. 2003) and in the RIXOS survey (Mason et al. 2000). In the optical follow-up of the former, spectroscopic redshifts of 0.180 and 0.256 were derived for WJ943.7 and WJ943.5, respectively.

In §2 we describe the data preparation, §3 deals with the methods and results of the spatial and spectral analysis of the groups, while §4 describes results and §5 implications of the mass analysis. A summary is presented in §6.

We adopt a cosmology with $\Omega_m = 0.3$ and $\Omega_\Lambda = 0.7$, and write the Hubble parameter as $H_0 = 100h$ km s⁻¹ Mpc⁻¹.

2 OBSERVATIONS AND DATA REDUCTION

WARPJ0943.7+1644 and WARPJ0943.5+1640 were observed by *XMM-Newton* in two separate observations for a total exposure time of 22 ks. All detectors were in Full Frame mode, and a medium optical blocking filter was used due to the presence of nearby bright stars.

Data preparation was carried out using the XMMSAS v5.3 software. Screening for periods of high background was performed by inspection of lightcurves extracted in the 10–

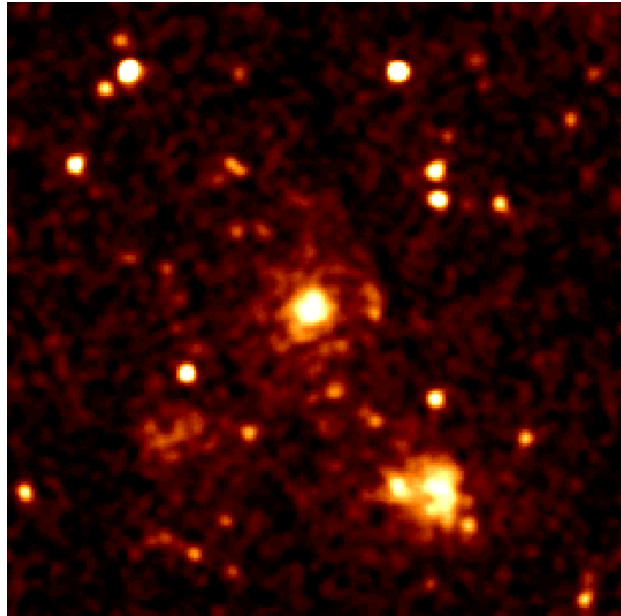


Figure 1. Combined (pn+2MOS) 0.4–2.5 keV photon count image after initial data filtering. The central 15×15 arcmin² is shown, smoothed with a Gaussian of 10 arcsec (FWHM). North is up and East is to the left. WJ943.7 is the central extended source, while WJ943.5 is seen roughly 5 arcmin to the South-west.

12 keV (for MOS) and 12–15 keV (pn) bands. Periods with count rates in excess of 0.15 cts s⁻¹ for MOS1/2 and 0.22 cts s⁻¹ for pn were removed. The second of the two observations was heavily affected by periods of high particle background. Screening for this left 7.7, 14.5, and 14.4 ks of useful exposure time for the pn, MOS1, and MOS2 cameras, respectively, in the first observation, while the corresponding values for the second observation were 1.0, 4.7, and 4.6 ks.

2.1 Imaging

Fig. 1 shows an image in the 0.4–2.5 keV band after the initial data filtering. Bright point sources were subsequently identified with XMMSAS and excised using an exclusion radius of 25 arcsec. Images were background subtracted prior to analysis as follows. For each instrument and observation, a blank sky background event file (Lumb 2002) was generated which had undergone identical lightcurve filtering to the data, and had been coordinate transformed to match the aspect solution of the latter. This ensured that the same CCD regions were considered when comparing background levels in our data and the blank sky files. The blank sky background was then determined in the 9–12 keV band within an annulus of inner radius 9 arcmin and outer radius 11 arcmin, and an analogous estimate was made for our data. Comparing the two background levels yielded a scaling factor f between the high-energy background in the current observations and in the blank sky data. The *total* background of the latter was then scaled accordingly and subtracted from the data.

At energies $E \lesssim 1.5$ keV, the resulting images may still contain a contribution from the soft X-ray background,

which is known to vary considerably with sky position and is not necessarily well represented by the blank-sky data for a given observation. The soft ($E < 2$ keV) photon excess of the resulting images relative to the blank-sky background was therefore determined in a large-radius (9–11 arcmin) ‘source-free’ annulus and subtracted from the images after correction for vignetting. This excess was found to be negative, i.e. a deficit of soft emission relative to the blank sky files is present in the data, constituting on average ~ 11 per cent of the total background over the entire field of view (a deficit might be expected, as the value of absorbing hydrogen column density N_H is on average a factor of ~ 2 lower in the Lumb background data than at the position of our pointing).

Note that all subsequent analysis, including investigation of source spectra, was restricted to energies $E \geq 0.4$ keV, for which the effective-area difference is negligible between the thin optical filter used for the Lumb (2002) data and the medium filter applied in our observations.

2.2 Spectra

A similar approach to the above was used for the removal of background in extracted spectra. Using the scaling factors f derived above, source spectra were created, and scaled blank-sky spectra extracted from the same (detector) region were subtracted for each instrument and observation. Large-radius (9–11 arcmin) source-free spectra were also created from the data and associated scaled blank-sky spectra were subtracted, the result reflecting the spectrum of any remaining soft background component due to the particular position on the sky. These residual spectra were finally also subtracted from the source spectra. All results from spectral fitting presented in this paper are based on this method for background subtraction, using the Lumb (2002) data as background templates. However, as a check on the robustness of our results, comparisons were made with results from two other methods for background subtraction. One is identical to the above, but uses another set of blank-sky background data also assembled from pointed observations (Read & Ponman 2003). These background data have the advantage of having been obtained with the medium blocking filter, allowing a test for any effect which might arise from using the thin-filter Lumb (2002) data for background subtraction in our medium-filter observations. The other method involves a simple local background subtraction, extracting background spectra in a 9–11 arcmin annulus in the source data. This ensures that the effect of any discrepancy between absorbing hydrogen column density and optical filter in source and background data can be tested, but it does not account for chip-to-chip variations in response or background level. We find that these two alternative methods produce results for the derived parameters which are consistent within 1σ with those obtained from the adopted approach. We therefore take our spectral results to be fairly robust.

3 DATA ANALYSIS

3.1 X-ray/optical identification and morphology

As is readily apparent even in the raw imaging data (Fig. 1), there is evidence for a third extended source in the field in addition to the two WARPS groups: To the South-east of the optical axis, faint extended emission is seen which was apparently not detected in *ROSAT* pointings and is consequently not included in any *ROSAT*-based source catalogues. We shall refer to this source as XMMJ0943.9+1641.

To determine the detailed X-ray morphology of these three systems as seen by *XMM*, images were produced for each instrument and observation in the 0.4–2.5 keV band (chosen to optimize S/N on the basis of extracted source spectra, see § 3.3), from which a combined, background subtracted, and exposure corrected image was made. Fig. 2 shows resulting X-ray surface brightness contours of the general region surrounding WJ943.7 and of the three extended sources in the region. Individual source contours are overlaid on optical images; where possible, we have used the follow-up imaging data from the WARPS survey itself.

To aid in investigating the nature of optical sources in the fields, and since spectroscopic results for the two groups are not available in the literature, the online near-infrared (*JHK* bands) catalogue of the 2 Micron All Sky Survey (2MASS) and its listing of associated optical sources in the Sloan Digital Sky Survey was employed. From the aperture magnitudes of the sources, colour-magnitude diagrams for all sources within $0.7h^{-1}$ Mpc of the X-ray centroid were produced (approximately the virial radii of the systems, see §4, corresponding to angular scales of 5.5 arcmin at $z = 0.18$ and 4.1 arcmin at $z = 0.256$. For XMMJ0943.9+1641 a radius of 4.0 arcmin was conservatively used). Colours were compared to those expected for a population of passively evolving early-type cluster galaxies of various metallicities at the appropriate redshift (Kodama & Arimoto 1997). A formation redshift of $z_f = 3$ was assumed, but results are essentially insensitive to realistic values of this parameter. It is worth keeping in mind when distinguishing between pointlike and extended NIR sources in the 2MASS catalogue that the point spread function (PSF) of the 2MASS telescopes is 2.5 arcsec at FWHM, corresponding to $\sim 5h^{-1}$ and $\sim 7h^{-1}$ kpc at the redshifts of WJ943.7 and WJ943.5, respectively. At faint NIR fluxes, a source classified as pointlike could thus potentially be a galaxy, if only the central bulge is detectable.

3.1.1 WJ943.7

WJ943.7 was selected for this study in part on the basis of its seemingly relaxed morphology in *ROSAT* PSPC observations. The overall structure of the X-ray emission is indeed seen from Fig. 2 to be fairly symmetric, supporting the assumption that the system is reasonably relaxed.

The position of the X-ray peak and centroid at ($\alpha = 09^h43^m44^s.6$, $\delta = +16^\circ44'25''$) coincides with that of an optical source, clearly identified as a galaxy upon inspection of the image. No optical identification of this galaxy could be secured from the LEDA or NED online databases. Its *R*-band apparent magnitude in the 2MASS catalogue is $m_R = 16.0$, making it the brightest galaxy in the field shown

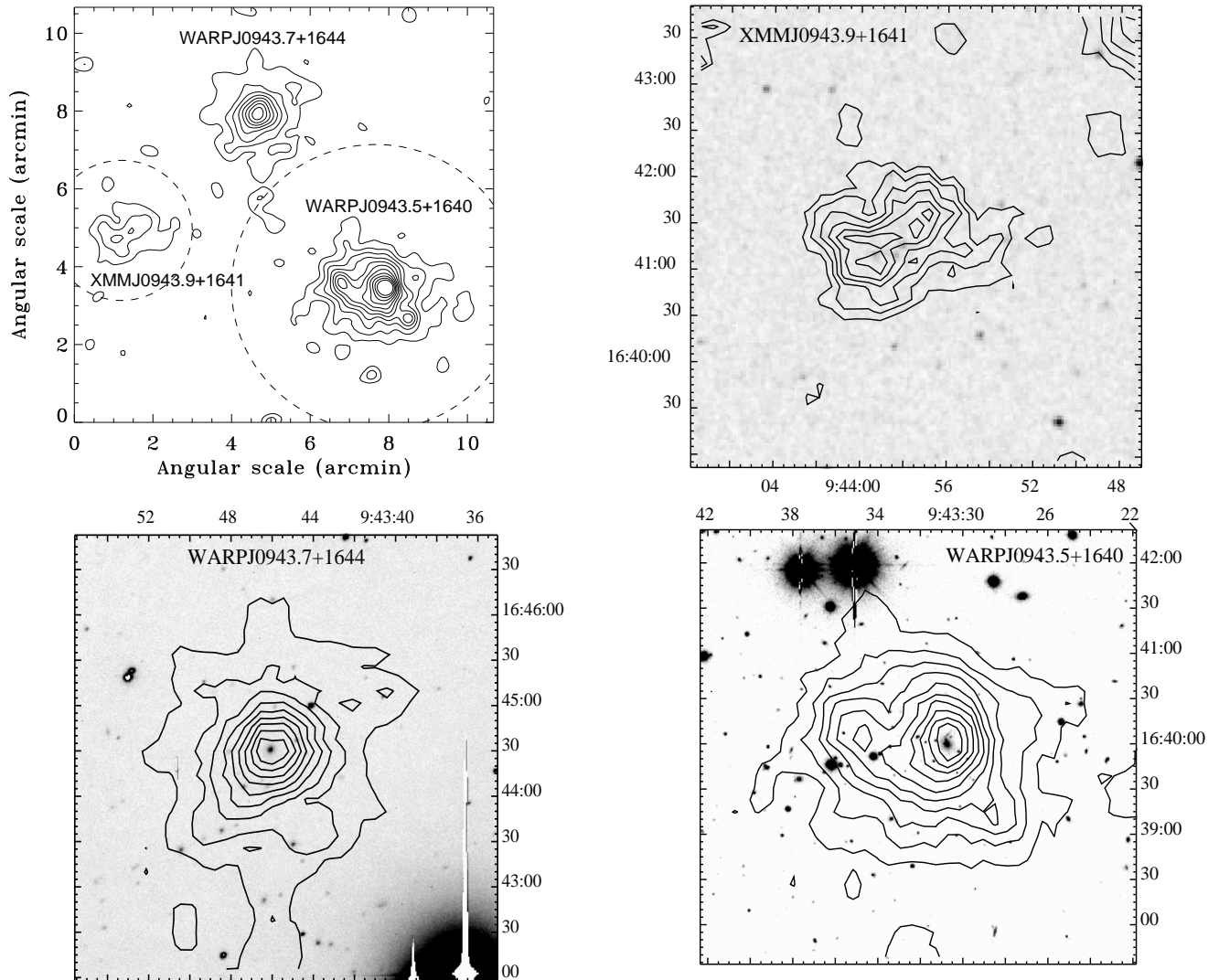


Figure 2. *Top left:* 0.4–2.5 keV surface brightness contours of the combined (pn+2MOS) background-subtracted and exposure-corrected image, binned to a spatial scale of $4 \text{ arcsec pixel}^{-1}$ and smoothed with a 20 arcsec Gaussian (FWHM). Dashed circles mark the exclusion regions invoked for the surface brightness and spectral analysis of WJ943.7 (see text). *Top right:* Smoothed and linearly spaced contours ($0.6\text{--}3 \times 10^{-5} \text{ cts s}^{-1} \text{ pixel}^{-1}$) of XMMJ0943.9+1641 overlaid on a $5 \times 5 \text{ arcmin}^2$ optical image from the Digitized Sky Survey. *Bottom panel:* Contours for WJ943.7 (0.6–6 in the above units) and WJ943.5 (0.8–8), overlaid on WARPS survey *I*-band and *R*-band image, respectively, taken with the 1.3-m McGraw-Hill telescope at MDM Observatory (images courtesy of G. Wegner and H. Ebeling).

in Fig. 2. Assuming an early-type galaxy spectrum and accounting for k -correction (Poggianti 1997) and Galactic extinction (Schlegel, Finkbeiner & Davis 1998), this translates into $M_V \approx -22.9$ ($h = 0.7$), which is indeed consistent with expectations for a bright elliptical. The source displays extended (7 arcsec) NIR emission in the 2MASS data and we find that its B - K , J - K , and H - K colours are perfectly consistent with an elliptical galaxy at the spectroscopic redshift. A total of four additional extended NIR sources are found within $0.7h^{-1} \text{ Mpc}$, of which two have colours very similar to those of the central source. These four sources span an R -band apparent magnitude range of $m_R = 16.8\text{--}18.1$. The bright source to the North-west of the X-ray centroid is a star.

3.1.2 WJ943.5

This source was similarly detected in both the CfA 160 deg² (Vikhlinin et al. 1998) and RIXOS (Mason et al. 2000) surveys. In contrast to WJ943.7, the X-ray emission of WJ943.5 clearly seems elongated in the NE–SW direction. The question is whether this apparent elongation is partly or entirely due to the presence of two nearby point sources (most clearly seen in the top left of Fig. 2), in particular the one East of the emission peak. We will return to this issue in §3.2 and §3.3. Nevertheless, the overall structure of emission appears slightly less relaxed than for WJ943.7.

Again, the position of the X-ray peak at ($\alpha = 09^h 43^m 31^s.0$, $\delta = +16^\circ 39' 57''$) (displaced $\sim 15 \text{ arcsec}$ to the

W with respect to the X-ray centroid) coincides with an optical source. The deep optical exposure shown in Fig. 2 allows us to readily identify it as an early-type galaxy. It is not listed in LEDA or NED but features an extended counterpart in the 2MASS data, this being however the only extended NIR source within $0.7h^{-1}$ Mpc. Its colours are in good agreement with those expected for a cluster elliptical at $z = 0.2 \sim 0.3$. Investigation of the image picks up at least a handful of more galaxies within the region marked by the X-ray contours, none of which have a NIR counterpart in the 2MASS data. This is not surprising, however, as the 2MASS nominal survey completeness limits are $m_J = 15.8$, $m_H = 15.1$, and $m_K = 14.3$ mag (for pointlike sources), thus rendering the detection of $L < L^*$ galaxies at $z = 0.256$ rather unlikely. The two optically bright sources within ~ 1 arcmin East of the centre are stars.

Regarding the two X-ray point sources, faint optical sources are present at the position of both, but neither display detectable NIR emission in the 2MASS data. As will be discussed, X-ray spatial and spectral analyses suggest that the Western source is truly pointlike, whereas the Eastern source might contain an extended component. In all subsequent analysis both sources were masked out, adopting exclusion radii of 25 arcsec and 40 arcsec for the Western and Eastern source, respectively. These choices will be justified in §3.2 and 3.3.

3.1.3 XMMJ0943.9+1641

As already mentioned, this source was not identified in *ROSAT* pointings. We regard the identification of the source in these data as secure, with the innermost contour in Fig. 2 being 8σ above the residual background. While no clear emission peak is identifiable, the X-ray centroid is found to be at ($\alpha = 09^h 43^m 58^s.5$, $\delta = +16^\circ 41' 17''$). The structure of emission seems quite disturbed, but deeper observations are required to firmly establish its X-ray morphological details.

Inspection of the 2MASS catalogue and Fig. 2 revealed evidence for four NIR/optical sources within the region covered by the displayed X-ray contours, of which only one is classified as extended in the infrared (roughly 0.7 arcmin from the X-ray centroid). None of these sources stand out as a bright central galaxy. They all have very similar colours, consistent with those of a cluster population at redshifts between 0.1–0.4 (with perhaps the upper value being more likely, given the optical and X-ray faintness of the region relative to the two WARPS groups). A second extended NIR source is present, but at a centroid distance of ~ 3 arcmin to the NW, it might rather be associated with WJ943.7.

3.2 Surface brightness distribution

3.2.1 One-dimensional profiles

The radial surface brightness profiles of the two WARPS groups were initially parametrized by fitting standard β -models, eq. (1), to the azimuthally averaged exposure-corrected emission, including a spatially uniform residual background. To minimize contamination from the other two extended sources in the field, exclusion regions for each of these were defined at their respective emission centroids (see

Fig. 2 for an example). A residual background level was determined, and fitting was done through adaptively binning the brightness profile such that each radial bin contained emission at $\geq 4.5\sigma$ above this background; this allowed an estimate of the maximal extent of emission while at the same time ensuring the presence of at least 20 source counts per bin (justifying the use of χ^2 statistics for fitting).

The resulting radial profiles and best-fitting β -models are shown in Fig. 3, and in Table 1 below we list the derived best-fitting parameters for both groups. Emission at $\geq 4.5\sigma$ is detected out to at least 3 arcmin in both cases, and the fits are acceptable, with reduced $\chi^2 = 0.94$ and 0.86 for 8 and 10 degrees of freedom (d.o.f.), respectively. Neither system shows evidence for any significant large-radius departure from the β -model or excess emission in the centre indicating a cooling flow. Note that WJ943.5 is detected to a smaller radius than WJ943.7, although it displays a higher central surface brightness. This reflects its larger β and hence fainter fluxes at sufficiently large radii. For XMMJ0943.9, emission at $> 4.5\sigma$ was detected out to ~ 75 arcsec but statistics were too poor to obtain useful constraints from a β -model fit.

The gas density profiles in groups must break from a power law decline at sufficiently large radii. Cosmological simulations which include only gravity and shock heating, produce clusters in which the gas density distribution follows that of the dark matter, and steepens progressively towards an r^{-3} dependence at large radii (NFW; Eke, Navarro & Frenk 1998; Frenk et al. 1999). Motivated by this, we also fitted a gas density profile of the NFW form, eq. (2), to the surface brightness profiles. Since there is little evidence for non-isothermality in the two groups (§3.3), we assumed X-ray emissivity $\propto n_e^2$, where n_e is the electron number density. For a profile of the form of eq. (2), the resulting line of sight projection S_{NFW} is not analytically tractable. Hence the fit was done by performing χ^2 -minimization on a grid of numerical profiles.

At large radii ($r \gg r_s$), $S_{\text{NFW}} \propto r^{-4}$, which is clearly much steeper than the dependence revealed by Fig. 3. Large scale radii r_s are therefore anticipated in the fits, as are large discrepancies in the inner regions where the observed flat density cores are incompatible with the steep NFW behaviour. Consequently, the data points inside the best-fitting core radii of the β -models were excluded in the fits. For both groups, the isothermal NFW fits are good, yielding fit qualities comparable to those obtained using β -models, the fit being slightly better for WJ943.5 and slightly worse for WJ943.7 than a β -model fit. Thus, assuming isothermal gas, the data are in accordance with models where the gas density shows a progressively steepening power-law index, as it does for an NFW model. As will be shown in §4.1, the X-ray emissivity of the groups is independent of temperature to within ~ 5 per cent for the relevant range of parameters involved, so the above result applies even if the gas is moderately non-isothermal. However, the scale radii obtained are in all cases large: for WJ943.5 $r_s \sim 630h^{-1}$ kpc and for WJ943.7 $r_s \sim 850h^{-1}$ kpc (even larger than the derived r_{200} , cf. § 4). This corresponds to small concentration parameters $c = r_{200}/r_s < 1$, and is in apparent conflict with expectations from numerical simulations (NFW; Eke et al. 1998; Moore et al. 1998; Lewis et al. 2000) and other observations (e.g. Pratt & Arnaud 2003) which typically find $r_s \simeq 0.1\text{--}0.25r_{200}$ (i.e. $c \approx 4\text{--}10$) for the dark matter distri-

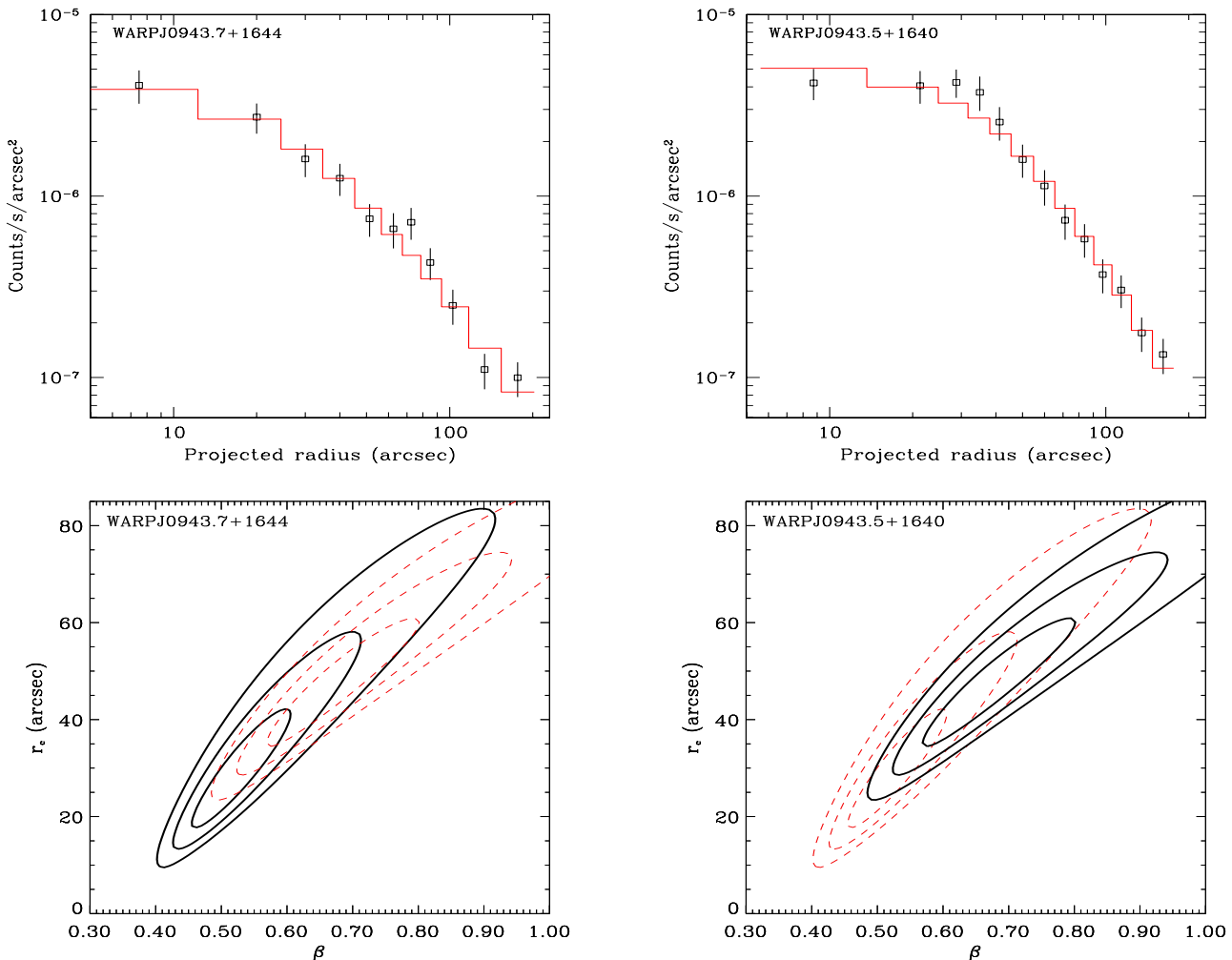


Figure 3. *Top:* Radial surface brightness profiles of WJ943.7 (left) and WJ943.5 (right), binned such that each bin contains emission at greater than 4.5σ significance. Also shown is the best-fitting β -model in each case. Error bars are 1σ . *Bottom:* Corresponding confidence contours ($1\sigma, 2\sigma, 3\sigma$) in the (β, r_c) plane. Solid (dark) contours describe those pertaining to the group itself, whereas dashed (light) contours describe those of the other group, overlaid for comparison. The same scales have been used in each panel for ease of comparison.

bution. Given that we are dealing here with the *gas* density, this most likely simply reflects the fact that the gas distribution is much less centrally concentrated than that of the dark matter, as will be substantiated in §5. Models in which gas traces total mass are hence clearly ruled out for both our groups. This is also supported by the results of Ettori & Fabian (1999), who use a similar approach for a sample of massive clusters, and find a mean ratio between NFW gas scale radius r_s and β -model core radius r_c of $r_s/r_c \approx 3$, whereas we find $r_s/r_c \gtrsim 15$ for WJ943.7 and $r_s/r_c \gtrsim 5$ for WJ943.5. Importantly, the large scale radii resulting from the fits also show that the derived surface brightness profiles are inconsistent with a steepening in the logarithmic density slope $\eta = -(\mathrm{d} \ln n_e / \mathrm{d} \ln r)$ towards $\eta \approx 3$ at large radii. In fact, the best-fitting NFW models produce slopes of $\eta = 1.66$ and 1.80 for WJ943.7 and $\eta = 1.87$ and 2.08 for WJ943.5 at the derived extent of emission r_{ext} (see Table 1 below) and at r_{200} (§4), respectively. For both groups, the concluding point is therefore that isothermal NFW models

only provide a good description of the data if the associated scale radii are so large as to make the resulting surface brightness profiles rather similar to β -models.

3.2.2 Two-dimensional profiles

Although the X-ray emission of both WARPS groups is reasonably symmetric and is well fitted by a one-dimensional β -profile, two-dimensional β -models were also fitted to the emission, using SHERPA, in order to further investigate the surface brightness structure. This approach has the advantage that the effects of the asymmetric EPIC PSF can be accurately taken into account in the model fit. However, whilst 2-D fitting takes better advantage of the available spatial information, the image counts do not satisfy the requirement of Gaussian errors which underlies the χ^2 statistic (the number of counts in some data bins may be very low). Following Helsdon & Ponman (2000), the maximum-likelihood based Cash statistic (Cash 1979) was used instead. Vignetting was

Table 1. Best-fitting values from 1-D and 2-D surface brightness fitting (0.4–2.5 keV). All uncertainties are 1σ for one interesting parameter. Physical scales are computed for distances corresponding to the spectroscopic redshifts of the groups. Radial extents r_{ext} specify the outer radius of the outermost radial bin containing a 4.5σ detection. Position angles are given counter-clockwise from the North. The goodness of fit for 2-D models is as described in the text.

1-D								
Source	Redshift	S_0 (cts s ⁻¹ arcsec ⁻²)	β	r_c (arcsec)	r_c (h ⁻¹ kpc)	$\chi^2/\text{d.o.f.}$	r_{ext} (arcsec)	r_{ext} (h ⁻¹ kpc)
WJ943.7	0.180	$4.18^{+1.02}_{-0.86} \times 10^{-6}$	$0.51^{+0.05}_{-0.04}$	$27.0^{+9.1}_{-6.5}$	57^{+19}_{-17}	7.5/8	200	425
WJ943.5	0.256	$5.33^{+0.72}_{-0.67} \times 10^{-6}$	$0.66^{+0.08}_{-0.06}$	$45.7^{+9.4}_{-7.7}$	127^{+26}_{-21}	8.6/10	175	490

2-D								
Source	S_0 (cts s ⁻¹ arcsec ⁻²)	β	r_c (arcsec)	r_c (h ⁻¹ kpc)	e	θ	Goodness of fit	
WJ943.7	$4.60^{+0.56}_{-0.50} \times 10^{-6}$	$0.49^{+0.03}_{-0.03}$	$24.9^{+4.2}_{-3.6}$	53^{+9}_{-8}	$0.00^{+0.07}_{-0.00}$	–	0.93	
WJ943.5	$5.93^{+0.37}_{-0.68} \times 10^{-6}$	$0.63^{+0.08}_{-0.03}$	$45.2^{+12.6}_{-4.1}$	126^{+35}_{-11}	$0.19^{+0.09}_{-0.04}$	81^{+8}_{-9}	0.16	

taken directly into account in the fit through including the exposure map in the modelling of the source.

The 2-D fit results are also presented in Table 1. For each source, the PSF model employed for convolution with the source model was produced at the relevant detector position at a photon energy of 1 keV using XMMSAS. Additional free parameters compared to the 1-D fit were the eccentricity $e \equiv (1 - b^2/a^2)^{1/2}$, position angle θ , and x - and y -centre of the X-ray gas distribution.

No estimator of the goodness of fit is immediately available when using the Cash statistic. Hence to address the issue of fit quality, we adopted a Monte Carlo approach, generating for each source 1000 artificial images based on the best-fitting model. In each case, Poisson noise was added to the input model image, which was subsequently convolved with the PSF model and vignetted. Model fits were then performed to these images in the same manner as for the real data, recording for each fit the value of the Cash statistic, and finally fitting a Gaussian to the resulting distribution of these values. Comparing the Cash statistic, C , derived for the real data to this distribution, a measure of the goodness of fit was obtained as the number of standard deviations σ separating C from the centre of the distribution. This value is also presented in Table 1, and it is seen that both fits are reasonably good, being less than 1σ from the distribution centre. Note also that confidence intervals can be assessed as for χ^2 statistics, since *differences* in the Cash statistic are χ^2 -distributed.

For both groups, the 1-D and 2-D results agree well within the errors. For WJ943.7, the derived β -value is typical for groups and poor clusters with X-ray temperatures below 1–2 keV. The X-ray morphology is consistent with zero eccentricity, and θ is therefore unconstrained for this source. WJ943.5, in contrast, appears to display a larger X-ray core and a β -value more typical of richer clusters ($T \gtrsim 3$ keV). The derived eccentricity of its X-ray emission, $e \approx 0.2$, is consistent with typical values found for other groups and clusters (Mohr et al. 1995; Helsdon & Ponman 2000). *ROSAT* results for other groups (Mulchaey & Zabludoff 1998) have shown that the optical light of the brightest

group/cluster galaxy is often well aligned with the position angle of the X-ray emission. In the case of WJ943.5, however, the X-ray position angle $\theta_X \sim 80^\circ$ seems not particularly well aligned with the R -band optical light of the central galaxy, which shows $\theta_{opt} \sim 50^\circ$. In the central regions, within 1 arcmin of the emission peak, the X-ray contours are nearly circular ($e \approx 0.02$), but the best-fitting position angle of $\theta_X \sim 20^\circ$ is effectively unconstrained and so is consistent with both of the above values.

The difference in r_c , and particularly β , seen for the two groups is interesting, inasmuch as the systems have reasonably similar temperatures (§3.3) and hence masses. To investigate the significance of the difference, we also plot in Fig. 3 the derived confidence contours in the (β, r_c) plane for both groups. Although the 1σ contours marginally overlap, it is clear that the two profiles are not consistent at 1σ . For WJ943.5, any combination of r_c and β leading to a typical group value of $\beta \lesssim 0.5$ is only marginally allowed within 3σ confidence. It could of course be conjectured that some process has lead to a significantly larger X-ray core for this group, which, given the quality of the data, naturally forces β towards high values in the fits. Another possibility is related to the fact that when masking out the Eastern point source seen in Fig. 2 to the standard radius of 25 arcsec, resulting residuals from 2-D surface brightness fitting suggest the source is not quite pointlike (whereas the W source is well accounted for by point source emission). This was confirmed by explicitly including, in the overall fit to the group emission, a point source model at the position of the E source, the result still showing systematic residuals around the source. The results listed in Table 1 are therefore based on an exclusion radius of 40 arcsec for this source, estimated from the 2-D fitting residuals to mask out the excess emission to sufficient accuracy. Furthermore, as will be described below, spectral results also suggest that the Eastern source is not pointlike. If indeed a ‘separate’ extended component is present at ~ 1 arcmin East of the group emission centroid, this might also drive r_c , and hence β , towards high values in the fits.

We note that an eccentricity of ~ 0.2 persists when

explicitly including the Eastern source in the 2-D modelling, either as pointlike or extended. This strongly suggests that the derived elongation and position angle of the group X-ray contours are intrinsic and not caused by excess emission from an extended source embedded in the group emission.

3.3 X-ray temperatures

For the spectral analysis, integrated spectra of the WARPS groups out to r_{ext} were extracted for each instrument and observation, accumulating the spectra in bins containing at least 20 counts. For each source, all six background-subtracted spectra were then fitted simultaneously in the 0.4–4 keV band, using an absorbed *mekal* model in XSPEC v11.1, with the redshift fixed at the spectroscopic value and N_H fixed at the Galactic value of $3.2 \times 10^{20} \text{ cm}^{-2}$ (Stark et al. 1992). Free parameters were thus temperature, metal abundance, and spectral normalization. Results are presented in Table 2, with metallicities derived using the solar abundance table of Anders & Grevesse (1989). Acceptable fits were obtained, with best-fitting temperatures and abundances characteristic of X-ray bright groups or poor clusters.

For WJ943.5 it was found that the spectrum could only be adequately fitted by one thermal component, provided the Eastern point source was excised out to at least 40 arcsec, once again suggesting that this source is extended rather than pointlike. The combined spectrum of the two ‘point’ sources seen in the group is nevertheless well modelled by a power-law of slope 1.8 ± 0.2 added on top of the thermal plasma spectrum of the intragroup medium. However, masking out the Western source and modelling the Eastern alone along with a thermal plasma representing the group emission, we find that in all cases marginally better fits are obtained when replacing the power-law model with another *mekal* thermal plasma at the group redshift, fixed at a metallicity of $0.3Z_\odot$. We find no evidence that the source is rather described by multiple power-laws or a single power-law with internal absorption. Allowing the redshift of the *mekal* model to vary yields z in the interval 0.2–0.3, i.e. consistent with the group redshift. These conclusions apply independently of the exact choice of fitting region, and seem to suggest the presence of a separate blob of plasma at a temperature roughly 0.5 keV hotter than the surrounding medium. Due to the limits on the data, a hardness map does not provide any additional information in this context.

For XMMJ0943.9, we also attempted to fit a thermal plasma model to the 0–75 arcsec spectrum, keeping temperature, redshift, and normalization as free parameters, while fixing the abundance at $0.3Z_\odot$. A *mekal* model provides a good fit ($\chi^2 = 20.9$ for 23 d.o.f.), yielding $T = 1.40^{+0.22}_{-0.18}$ (1 σ errors) and a redshift of $z = 0.33^{+0.06}_{-0.07}$ (90 per cent confidence). With both parameters reasonably well determined, this suggests that XMMJ0943.9 is a yet more distant galaxy group. The derived redshift is in good agreement with that expected from the optical-NIR colours of sources in this region, cf. §3.1. We derive an unabsorbed 0.5–2 keV flux of $\sim 3 \times 10^{-14} \text{ ergs cm}^{-2} \text{ s}^{-1}$, corresponding to a luminosity of $1.0 \times 10^{43} h^{-2} \text{ ergs s}^{-1}$ at the nominal best-fitting redshift.

Due to the limited statistics available (we record ~ 1500 and ~ 1100 background-subtracted source counts for WJ943.7 and WJ943.5, respectively, within the non-excluded regions), a detailed study of temperature and

Table 2. Results of *mekal* fits to the integrated 0.4–4 keV spectra, with N_H fixed at the Galactic value of $3.2 \times 10^{20} \text{ cm}^{-2}$. Luminosities are given in the 0.5–2 keV band in units of $10^{43} h^{-2} \text{ ergs s}^{-1}$ (see text for details). Errors are 1 σ for one interesting parameter.

Source	T/keV	Z/Z_\odot	χ^2/dof	L_X (10^{43} erg/s)
WJ943.7	$1.67^{+0.12}_{-0.15}$	$0.34^{+0.12}_{-0.11}$	164/168	$0.57^{+0.07}_{-0.07}$
WJ943.5	$2.40^{+0.40}_{-0.39}$	$0.31^{+0.24}_{-0.16}$	126/122	$1.97^{+0.25}_{-0.25}$

abundance gradients in the intra-cluster medium (ICM) is not feasible. Although a hardness map does not reveal evidence for any significant temperature variations within either group, an examination of the gross structure of the ICM temperature distribution $T(r)$ in the two groups was nevertheless attempted by extracting spectra in two or three concentric annuli, containing roughly equal numbers of source counts. The spectra were then fitted as above, with abundances fixed at the value derived from the fits to the integrated spectra inside r_{ext} (consistent results for both T and Z were obtained when the latter was allowed to vary). In all bins good fits are obtained, and results for two bins are shown in Fig. 4. Although both groups show tentative evidence for a mild ($\sim 0.5 - 1 \text{ keV}$) temperature decline with radius, the ICM is consistent with being isothermal within the 90 per cent confidence (1.65σ) errors in each bin. Specifically, there is no indication of the presence of cool cores in the central regions. This is consistent with the lack of excess emission in the group cores relative to the best-fitting isothermal β -model. When spectral properties are derived using three rather than two annuli, these are, of course, subject to larger statistical uncertainties, but are again consistent with isothermality, and show no central cooling.

3.4 X-ray fluxes and luminosities

From the best-fitting *mekal* models for the integrated spectra, resulting 0.5–2 keV unabsorbed fluxes for WJ943.7 (WJ943.5) are $0.96^{+0.11}_{-0.12} (1.12^{+0.14}_{-0.14}) \times 10^{-13} \text{ ergs cm}^{-2} \text{ s}^{-1}$ within the regions adopted for spectral fitting. Errors were determined from the fractional errors on the spectral normalisation. Correcting the WJ943.5 flux inside the spectral region for removed area, assuming the nominal best-fitting 2-D β -model in Table 1, the resulting flux is $1.43^{+0.19}_{-0.18} \times 10^{-13} \text{ ergs cm}^{-2} \text{ s}^{-1}$, where the quoted 1 σ errors are from the spectral flux determination alone.

At the relevant redshifts, the derived fluxes within r_{ext} correspond to unabsorbed 0.5–2 keV restframe luminosities of $L_X = 0.57^{+0.07}_{-0.07} \times 10^{43} h^{-2} \text{ ergs s}^{-1}$ (WJ943.7) and $1.97^{+0.25}_{-0.25} \times 10^{43} h^{-2} \text{ ergs s}^{-1}$ (WJ943.5, corrected for removed area as above), as listed in Table 2. In Fig. 5 the best-fitting T_X and the bolometric (0.01–15 keV rest-frame) luminosities within the radii adopted for spectral fitting are compared to those of the low-redshift ($z < 0.04$) $T \geq 1 \text{ keV}$ groups in the samples of Helsdon & Ponman (2000) and Xue & Wu (2000). Note that both depicted $L_X - T$ relations for groups ($L_X \propto T^{4.9 \pm 0.8}$, Helsdon & Ponman 2000; $L_X \propto T^{5.57 \pm 1.79}$, Xue & Wu 2000) have been derived using groups at ‘all’ T , whereas only groups with $T \geq 1 \text{ keV}$ are

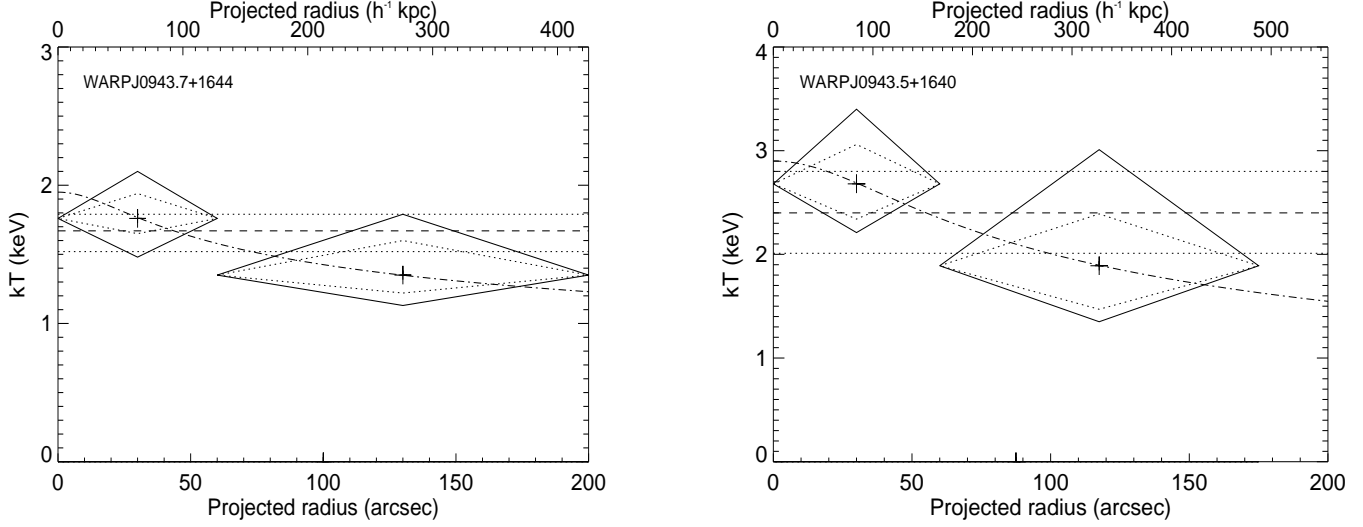


Figure 4. Projected radial variation of the X-ray gas temperature in WJ943.7 (left) and WJ943.5 (right). Crosses mark the best-fitting values in each bin, with surrounding solid (dotted) lines showing the 90 per cent (1σ) confidence intervals. Dashed horizontal lines show the best-fitting value from the integrated spectrum, with the associated 1σ errors marked by dotted lines. The dot-dashed curves represent the polytropic models discussed in the text.

included in Fig. 5. Note also that while the groups in the Helsdon & Ponman sample were analysed in a coherent manner, data for the Xue and Wu groups were compiled from a number of different sources. In neither case was the X-ray emission of the groups derived within a consistent radius, be it physical or as a fraction of r_{200} , and thus a rigorous comparison to our results cannot be made. Nevertheless, it is found that both WARPS groups have luminosities consistent with those derived for other poor clusters, agreeing well with the cluster $L_X - T$ relation of slope 2.79 ± 0.08 derived by Xue & Wu (2000). This $L_X - T$ relation is based on a sample of 274 clusters drawn from the literature, the large majority of which are at $z < 0.5$, and agrees well at the relevant temperatures ($1 \lesssim T \lesssim 3$ keV), with, e.g., the low-to-moderate redshift ($z < 0.2$) relation derived for the $T > 1$ keV WARPS clusters (Fairley et al. 2000) and with estimates for $z < 0.1$ clusters from *BeppoSAX* data (Ettori, De Grandi & Molendi 2002).

4 MASS ANALYSIS

4.1 Effects of non-isothermality

It is clear from Fig. 4 that the temperature profiles are not resolved with sufficient accuracy to immediately allow detailed profiles to be made of temperature-based quantities such as mass or gas mass fraction. Fig. 4 and the ensuing discussion shows, however, that there is no evidence for significant departures from isothermality in either group at any radius probed, and an isothermal distribution is, indeed, the flattest reasonable temperature distribution with which the data are consistent. One might argue that T in the innermost bin could have been underestimated due to the presence of a cooling flow; this would produce a steeper temperature profile outside the cooling core and hence a larger deviation from isothermality than is immediately apparent in Fig. 4. While the expected central cooling times

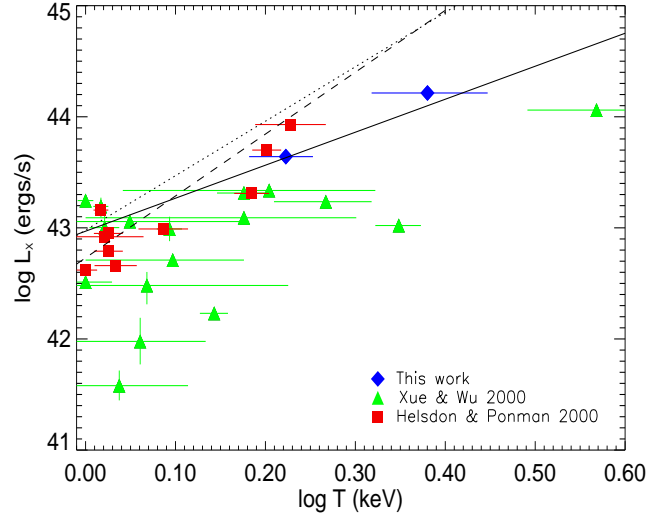


Figure 5. The derived bolometric luminosities and temperatures of the two WARPS groups (diamonds), shown together with the values for the $T \geq 1$ keV groups of Xue & Wu (2000; triangles) and Helsdon & Ponman (2000; squares). Also shown is the nominal best-fitting $L_X - T$ relation for *all* groups in the samples of Xue & Wu (dashed line), Helsdon & Ponman (dotted line), and for the cluster sample of Xue & Wu (solid line). The figure assumes an Einstein-de Sitter cosmology with $h = 0.5$.

(using the cooling curves of Sutherland & Dopita 1993, for a $Z = 0.3Z_\odot$ plasma) of ~ 7 and ~ 11 Gyr for WJ943.7 and WJ943.5, respectively, may suggest the presence of weak cooling flows, this is not supported by the derived surface brightness profiles. Moreover, a number of recent studies of low-temperature systems with well-defined temperature profiles have demonstrated that, outside a possible cool core, isothermality may indeed be a good assumption

(e.g. Mushotzky et al. 2003; Pratt & Arnaud 2003). In the following sections we will therefore assume the ICM to be isothermal at the mean temperature derived inside r_{ext} . It is nevertheless instructive to consider the impact of assuming isothermality, in order to assess the potential error in doing so, and in all subsequent analysis we will attempt to quantify potential effects of this assumption on our results.

On the basis of the temperature data of Fig. 4, one can assume model profiles for $T(r)$ which (i) are consistent with the data, (ii) can be justified with reference to other observed and simulated systems, and (iii) can provide an indication of the systematic errors associated with making a single isothermal assumption for $T(r)$. Hence, in the absence of detailed temperature data, such model profiles are used in the following in conjunction with the isothermal assumption. We readily acknowledge the fact that the resulting radial variation of various quantities derived from $T(r)$ is, strictly speaking, modelled rather than observed, providing an approximation to the true profile which is only reliable to the extent to which the ICM temperature behaves as assumed. As will be seen, the overall conclusions are nevertheless not sensitive to specific choices for $T(r)$ allowed by Fig. 4.

The detailed shape of the temperature profile in our groups is largely unconstrained. There is, however, compelling evidence from both observations and simulations of groups and clusters that a polytropic equation of state,

$$T \propto \rho^{\gamma-1}, \quad (3)$$

provides a good description of any radial decline in gas temperature outside a possible cool core. This is the case both for simulated clusters (Lewis et al. 2000; Loken et al. 2002), simulated groups/cool clusters (Ascasibar et al. 2003), and for observed clusters with well-determined temperature profiles (e.g. Markevitch et al. 1998; Ettori & Fabian 1999; Markevitch et al. 1999; Pratt, Arnaud & Aghanim 2001; Pratt & Arnaud 2002) or surface brightness profiles (Miralda-Escude & Babul 1995). It is clearly also a better description than the isothermal assumption in some clusters with less well-determined temperature profiles (see e.g. Sarazin, Wise & Markevitch 1998). Eq. (3) is consequently employed here as a tool to investigate the systematic errors associated with assuming isothermality. For the temperature data shown in Fig. 4, polytropic models intercepting the nominal best-fitting temperature in each bin have indices of $\gamma = 1.15$ for WJ943.7 and $\gamma = 1.22$ for WJ943.5, very similar to values found for observed (Markevitch et al. 1999; Ettori & Fabian 1999) and simulated (Lewis et al. 2000; Ascasibar et al. 2003) clusters. Here we shall not attempt to include errors on these indices; given the available photon statistics, they would not be well constrained for the present data and their errors would propagate into large uncertainties on the resulting total masses.

If indeed the gas is polytropic, i.e. satisfying eq. (3), and if ρ follows a β -model, the true gas temperature T_{true} will differ from the projected (i.e. measured) one T_{proj} only by a constant factor,

$$\frac{T_{true}}{T_{proj}} = \frac{\Gamma[\frac{3}{2}\beta(1+\gamma)]\Gamma(3\beta - \frac{1}{2})}{\Gamma[\frac{3}{2}\beta(1+\gamma) - \frac{1}{2}]\Gamma(3\beta)} \quad (4)$$

(Markevitch et al. 1999), which amounts to 1.07–1.08 for the systems studied here. Strictly speaking, eq. (4) is only valid assuming emissivity $\propto n_e^2 T^\alpha$, but in the 0.4–4 keV

band considered for spectral fits, and over the relevant temperature ranges (1.3–2.0 keV for WJ943.7 and 1.6–2.9 keV for WJ943.5; see Fig. 4), the emissivity is temperature-independent to within 5 per cent and is $\propto T^\alpha$ to within 3 per cent for a $Z = 0.3Z_\odot$ mekal plasma.

4.2 Total masses and virial radii

Motivated by the regularity of the X-ray emission in the groups, we assume spherical symmetry and hydrostatic equilibrium of the X-ray emitting gas. The total gravitating mass inside a radius r is then given by

$$M_{grav}(< r) = -\frac{kT(r)r}{G\mu m_p} \left(\frac{d \ln \rho_{gas}}{d \ln r} + \frac{d \ln T}{d \ln r} \right), \quad (5)$$

where μ is the mean molecular weight and m_p is the proton mass. Numerical simulations (Evrard, Metzler & Navarro 1996) show that this is a reliable mass estimator out to at least r_{500} , the radius containing a mean overdensity of 500 with respect to the critical density $\rho_c(z)$, which is comparable to the extent of emission r_{ext} in both groups (see below). Taking $\mu = 0.6$ and using the emission-weighted mean temperatures given in Table 2, along with the derived parameters for the gas profiles, the resulting total masses within r_{ext} are presented in Table 3. Adopting a Monte Carlo approach, the associated uncertainties were estimated by constructing 10,000 artificial mass profiles. For each of these, the values of involved parameters (r_c , β , T) were taken from an asymmetric Gaussian distribution centered at the best-fitting value and having characteristic upper and lower widths given by the associated 1σ uncertainties (Tables 1 and 2). The derived distribution of masses was in general also an asymmetric Gaussian; the quoted mass errors are the associated standard deviations (upper and lower) with respect to the nominal best-fitting values.

Assuming the groups to be virialized out to r_{200} , the virial radius can be self-consistently computed from the derived mass profile once $\rho_c(z)$ is known. Using

$$\rho_c(z) = \frac{3H_0^2}{8\pi G} [(1+z)^3 \Omega_m + (1+z)^2 (1 - \Omega_m - \Omega_\Lambda) + \Omega_\Lambda], \quad (6)$$

where the term in brackets is the ratio $(H(z)/H_0)^2$, we derive nominal virial radii $r_{vir} = r_{200} = 0.57h^{-1}$ and $0.74h^{-1}$ Mpc for WJ943.7 and WJ943.5, respectively, in the adopted Λ CDM cosmology. We list r_{200} and r_{500} relative to r_{ext} in Table 3; it is seen that emission has been detected beyond r_{500} and out to 74 and 66 per cent of r_{200} in the two cases.

A temperature gradient in the X-ray gas changes total masses, and hence also r_{200} and r_{500} . Assuming the above polytropic gas profiles lowers the estimated masses within r_{500} and r_{200} by 9 and 20 per cent for WJ943.7 and 11 and 29 per cent for WJ943.5 (r_{500} and r_{200} themselves decrease by 3 and 7 per cent for WJ943.7 and 4 and 11 per cent for WJ943.5). Given that the fractional errors on these masses would be larger than for the isothermal case (because of errors on γ), the two scenarios produce masses consistent with each other within 1σ . Thus, within this statistical uncertainty the conclusions on M_{grav} remain unaffected by the presence of a temperature gradient.

4.3 Masses of X-ray gas

To determine gas masses in the groups, the normalisation of the gas density profile must be established. For an isothermal ICM, this can be directly derived from the best-fitting β -model for the surface brightness, using the spectral (in effect, luminosity) normalization in XSPEC,

$$A = 10^{-14} (4\pi(D_A(1+z))^2)^{-1} \int n_e n_H dV \text{ cm}^{-5}, \quad (7)$$

where D_A is the angular diameter distance to the source, and n_e and n_H are the number densities of electrons and hydrogen, respectively. With n_e and n_H following the best-fitting β -profile out to r_{ext} , their central values are found by evaluating the integral in eq. (7), assuming $n_e/n_H = 1.17$. We find very similar central electron densities $n_{e,0}$ for the two groups of $3.15 \pm 0.20 \times 10^{-3} h^{1/2} \text{ cm}^{-3}$ (WJ943.7) and $2.91 \pm 0.19 \times 10^{-3} h^{1/2} \text{ cm}^{-3}$ (WJ943.5), with errors obtained from the derived errors on the spectral normalization A . When converting these number densities to mass densities $\rho = n_e \mu_e m_p = n_H \mu_H m_p$, $\mu_e = 1.17$ and $\mu_H = 1.40$ was assumed, appropriate for a fully ionized $Z = 0.3Z_\odot$ plasma (e.g. Mohr, Mathiesen & Evrard 1999). The total gas masses are finally found by simple volume integration of $\rho(r)$ inside r_{ext} .

In the non-isothermal case discussed above, $M_{gas}(r)$ changes because the derived gas density depends on emissivity and hence temperature. To quantify the magnitude of this change, we took for each group the best-fitting isothermal spectral models within r_{ext} and changed the associated temperature within its extreme polytropic values at $T(r=0)$ and $T(r=r_{ext})$ (cf. Fig. 4), corrected to the 'true' value via eq. (4). This was done subject to the constraint that the total 0.4–2.5 keV flux, from which the surface brightness profile has been extracted, should remain constant. The resulting change in spectral normalisation A then translates, via eq. (7), into a maximum resulting error on the central gas density and hence total gas mass. In all cases, these changes were found to be less than 5 per cent within r_{ext} relative to the isothermal case, i.e. lying within the 1σ statistical uncertainties from the spectral fits. We therefore assumed in the following that M_{gas} remains unaffected by a change to the polytropic models.

5 DISCUSSION

5.1 Gas mass fractions

The resulting gas mass fractions $f_{gas} = M_{gas}/M_{grav}$ within r_{ext} and r_{500} are also presented in Table 3, along with the values resulting from extrapolating out to r_{200} . The associated errors were obtained from M_{gas} and M_{grav} using standard error propagation. For comparison with previous work on the topic, we note that the derived gas mass fractions within (r_{500}, r_{200}) correspond to $(0.049, 0.065)h^{-3/2}$ (WJ943.7) and $(0.060, 0.072)h^{-3/2}$ (WJ943.5) for a flat standard CDM universe, and $(0.053, 0.070)h^{-3/2}$ (WJ943.7) and $(0.067, 0.079)h^{-3/2}$ (WJ943.5) for an open CDM universe with deceleration parameter $q_0 = 0$. Based on a coherently analysed sample of 66 systems ranging from individual galaxy haloes to massive clusters ($T = 0.5\text{--}17$ keV), Sanderson et al. (2003) derive a mean gas fraction within r_{200} of

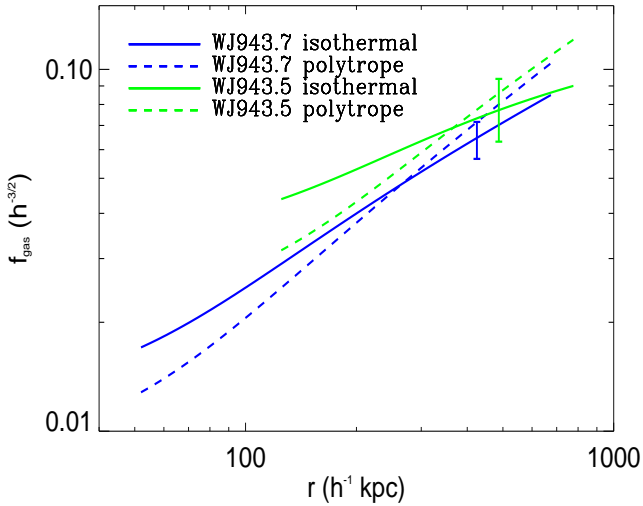
$\langle f_{gas} \rangle = 0.0785 \pm 0.006 h^{-3/2}$ (OCDM, $q_0 = 0$), with, in general, lower values for cool systems and a statistically significant trend of f_{gas} increasing with T , a trend which is, however, subject to considerable scatter. The two groups studied here seem to conform to this trend, with (in this particular $q_0 = 0$ cosmology) WJ943.5 lying close to this mean value and WJ943.7 having somewhat smaller f_{gas} . In any given cosmology, the derived nominal gas mass fraction for the WJ943.5 group is also found to be comparable to mean values reported for more massive clusters ($T > 4$ keV) by Ettori & Fabian (1999) and Castillo-Morales & Schindler (2003) and for intermediate-mass systems ($T = 2.5\text{--}5$ keV) by Mohr et al. (1999) and Arnaud & Evrard (1999). WJ943.7, however, displays a lower f_{gas} than found in these studies, with a value very similar to, e.g., that found for the $T \simeq 2$ keV cluster A1983 (Pratt & Arnaud 2003). For both groups, f_{gas} is found to be clearly smaller than the values obtained for massive ($T > 4$ keV) clusters (e.g., Mohr et al. 1999; Arnaud & Evrard 1999; Grego et al. 2001; Sanderson et al. 2003). In summary, within r_{200} WJ943.5 seems to be reasonably representative of the general cluster population, whereas f_{gas} of WJ943.7 is more typical of values reported for slightly less massive systems situated at the interface between groups and clusters.

Using the polytropic models, we find that f_{gas} is raised to 0.061 (0.086) within r_{500} (r_{200}) for WJ943.7, and 0.079 (0.107) for WJ943.5. These values are larger than the nominal isothermal values by 5 per cent within r_{500} and between 10 and 20 per cent within r_{200} . Even more so than for the total mass M_{grav} , they are comfortably consistent with the isothermal values within 1σ . We stress that, barring any additional systematic errors, our derived values within r_{200} should be fairly reliable, since they involve a relatively small degree of radial extrapolation compared to results for other groups. In this light it is interesting to note that our values are much closer to cluster values than often reported for small groups within smaller radii (e.g. David, Jones & Forman 1995; Pedersen, Yoshii & Sommer-Larsen 1997; Mohr et al. 1999; Mushotzky et al. 2003).

The modelled radial variation of f_{gas} in both groups is shown in Fig. 6. For the polytropic models, M_{grav} is lower at large radii, but r_{500} and r_{200} , within which M_{gas} is evaluated, also decrease. Since f_{gas} clearly increases with r even in the isothermal case, the relative impact of assuming a negative temperature gradient is therefore less pronounced at large radii for f_{gas} than for M_{grav} . The gas mass fraction of both systems increases out to the radii probed, with the standard implication that the intragroup gas is more extensively distributed than the dark matter. The consistency between the isothermal and polytropic models strongly suggests that when taking the errors into account, the overall radial behaviour of f_{gas} shown in Fig. 6 is a robust result. The strong dependence of f_{gas} on radius suggested by the figure, particularly for the cooler WJ943.7, is furthermore corroborated by the results of §3.2 for isothermal NFW fits to the surface brightness profiles, which, when scaled to r_c or r_{200} , show NFW scale radii for the gas much larger than those of simulated and observed hotter systems with a milder radial variation of f_{gas} (cf. Ettori & Fabian 1999). The weak temperature dependence of the emissivity in the relevant temperature and energy ranges (§4.1) implies that, within

Table 3. Derived gas masses, total gravitating masses, and gas mass fractions within the derived extent of emission r_{ext} , r_{500} , and the approximate virial radius r_{200} . All values are given in the adopted Λ CDM cosmology of $(\Omega_m, \Omega_\Lambda) = (0.3, 0.7)$.

Source	r_{ext}/r_{200}	r_{ext}/r_{500}	$M_{gas}(r_{ext})$ ($h^{-5/2} M_\odot$)	$M_{tot}(r_{ext})$ ($h^{-1} M_\odot$)	$f_{gas}(r_{ext})$ ($h^{-3/2}$)	$f_{gas}(r_{500})$ ($h^{-3/2}$)	$f_{gas}(r_{200})$ ($h^{-3/2}$)
WJ943.7	0.74	1.18	$2.47^{+0.16}_{-0.16} \times 10^{12}$	$3.82^{+0.36}_{-0.42} \times 10^{13}$	$0.065^{+0.007}_{-0.008}$	$0.058^{+0.007}_{-0.007}$	$0.077^{+0.009}_{-0.010}$
WJ943.5	0.66	1.07	$5.94^{+0.37}_{-0.40} \times 10^{12}$	$7.70^{+1.61}_{-1.32} \times 10^{13}$	$0.077^{+0.017}_{-0.014}$	$0.075^{+0.016}_{-0.014}$	$0.089^{+0.019}_{-0.016}$

**Figure 6.** Gas mass fraction f_{gas} plotted from r_c to r_{200} , using two assumptions for the temperature profile. Dark curves for WJ943.7, light curves for WJ943.5. Solid lines represent isothermal gas, dashed lines the polytropic models discussed in the text. Typical error bars for the isothermal case are shown at $r = r_{ext}$, beyond which f_{gas} is extrapolated.

the errors, this result holds equally well for the polytropic models.

5.2 Entropy

The entropy of the ICM, here defined as $S \equiv T/n_e^{2/3}$, reflects the accretion history of the hot gas and as such is a prime indicator of the physical processes involved in the formation and evolution of groups and clusters. Recent studies of the entropy in systems covering a wide range in masses have made it clear that gravity-driven processes alone cannot account for the observed entropy: Systems at all scales, most notably low-mass ones, show evidence for excess entropy relative to that expected from purely gravitational heating and compression of the gas.

Various mechanisms have been proposed to explain this excess entropy, see e.g. the discussion in Ponman, Sanderson & Finoguenov (2003). We note here that the rather large values of f_{gas} found for our systems seem inconsistent with cooling-only models, which require more than 50 per cent of the gas in low- T systems like these to cool out of the diffuse hot phase (e.g. Davé, Katz & Weinberg 2002; Ponman et al. 2003).

The radial variation of entropy cannot be computed in

a model-independent way for the two groups studied here, given the poorly resolved temperature profiles. Using instead the best-fitting β -models along with the isothermal assumption, resulting central entropies are 78 ± 8 and $118 \pm 20 h^{-1/3} \text{ keV cm}^2$ for WJ943.7 and WJ943.5, respectively, rising to 113 and $142 h^{-1/3} \text{ keV cm}^2$ at a fiducial radius of $0.1r_{200}$.

Self-similar scaling between systems of different masses would lead to $S \propto (1+z)^{-2} T$. In Fig. 7, modelled profiles of $S(r)$ are plotted for each group for both the isothermal and polytropic cases. The entropy has been scaled by $(1+z)^2/T$ so as to ‘remove’ the dependence on mass and redshift in the self-similar case. In this representation the profiles of the two groups are seen to be fairly similar. The flattening in the entropy profiles seen inside $0.1r_{200}$, due to the core in the gas density, is not a reliable result, since it is based on the assumption that $T(r)$ does not drop within the central $\sim 50 \text{ kpc}$. As can be seen from Fig. 4, our data do not allow us to resolve the temperature structure on such small scales. What is clear from our results, is that any isentropic core in these groups does not extend to $r \gtrsim 0.2r_{200}$, in contrast to the predictions of simple preheating models for such poor systems (Tozzi & Norman 2001; Babul et al. 2002; Voit et al. 2003). This is consistent with recent results for other groups (Mushotzky et al. 2003; Pratt & Arnaud 2003) and argues against significant preheating in a simple spherical collapse scenario.

Also plotted in Fig. 7 (triangles) is the expectation for S based on self-similar scaling of massive clusters (Ponman et al. 2003). For both groups, the scaled entropy exceeds that observed in massive clusters at $0.1r_{200}$. Further out our results are more uncertain, but the modelled profiles suggest that this excess seems to persist out to at least r_{500} , where the scaled (isothermal) entropies of the groups are a factor ~ 2 above the self-similar values. For our observed gas density profiles, the polytropic indices of both groups would have to be $\gamma \gtrsim 1.40$ in order to avoid excess entropy at r_{500} . This is well beyond the values of γ obtained for observed and simulated groups and clusters. The derived entropy levels at $0.1r_{200}$ and r_{500} , and hence the associated excesses with respect to the massive clusters of Ponman et al. (2003), are in good agreement with the best-fitting $S-T$ relations at the relevant radii of the *entire* group/cluster sample of Ponman et al. (2003).

Spherical shock heating models and most cosmological simulations produce entropy profiles with a power law form $S \propto r^{1.1}$ (e.g. Tozzi & Norman 2001). Two lines of this slope have also been plotted in Fig. 7. The lowest line, which agrees fairly well with the triangles representing observations of rich clusters, is normalised to the scaled mean value at r_{200} of the $M \simeq 5 \times 10^{14} h^{-1} M_\odot$ simulated ‘Santa Barbara’ cluster (Frenk et al. 1999), which included only gravitational physics. The profile has been scaled using an

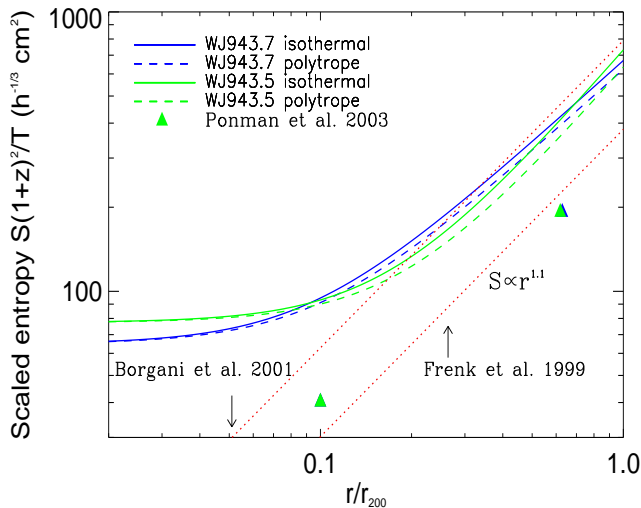


Figure 7. Scaled entropy $S(1+z)^2/T$ as a function of r/r_{200} , using two assumptions for the temperature profile. Triangles mark the expected values at $0.1r_{200}$ and r_{500} based on a self-similar scaling from the values observed in hot clusters. Sloping dotted lines represent the self-similar profile expected from shock heating in a spherical smooth accretion scenario, $S \propto r^{1.1}$, normalised at r_{200} to the preheated $T \approx 2$ keV cluster simulation of Borgani et al. (2001), and to the simulated $T \approx 6.5$ keV cluster of Frenk et al. (1999) which includes no heating or cooling effects.

estimated emission-weighted temperature of $T_{ew} = 6.5$ keV, derived from its mass-weighted value of $T_{mw} = 4.7$ keV assuming a ratio $T_{ew}/T_{em} \approx 1.4$, as suggested by results from simulations (Borgani et al. 2002) and observations (Sanderson et al. 2003). While only a suggestive result, this profile clearly fails to reproduce our modelled entropy levels at large radii. Also shown is an $S \propto r^{1.1}$ line normalised at r_{200} to the result obtained for a $T = 2.1$ keV cluster in numerical simulations of cluster formation by Borgani et al. (2001). These simulations include preheating at a level of $45h^{-1/3}$ keV cm², and do reproduce the large entropy excesses hinted at for our groups at r_{500} without forming a distinct isentropic core.

Whereas the absence of a large isentropic core is in direct conflict with simple smooth accretion of preheated gas, the excess entropy at large radii suggested by our analytical profiles may, in fact, be explained by such models (for details, see Voit et al. 2003 and Voit & Ponman 2003).

6 CONCLUSIONS

The main results of this work may be summarized as follows.

- Using sensitive *XMM-Newton* observations, we have mapped the X-ray emission out to, on average, 70 per cent of the estimated virial radii r_{200} in two X-ray selected galaxy groups at redshifts $z = 0.18$ and $z = 0.256$. We find the X-ray surface brightness profiles of both systems to be well described by standard β -models out to the radii probed, with indices of $\beta = 0.49$ and 0.63 . Fits to isothermal NFW profiles for the gas density indicate that the surface brightness data

do not rule out a steepening in the density profile at large radii as might be expected on physical grounds. However, adequate fits for such models can only be obtained with a very large scale radius, and models in which gas traces mass are strongly ruled out for both groups.

- Emission-weighted mean temperatures, determined within the same radii as the surface brightness profiles, are found to be $kT = 1.7 \pm 0.1$ and 2.4 ± 0.4 keV, with corresponding gas metallicities roughly 0.3 solar. The temperature profiles are poorly resolved but are consistent with isothermality within 90 per cent confidence.

- Radial profiles of gas mass, gravitating mass, and gas mass fraction have been determined assuming both isothermal and polytropic gas distributions allowed by the data. In both cases, the gas mass fraction clearly increases with radius, implying a more extended gas distribution than that of the total mass. Within the derived extent of emission, gas mass fractions are $0.065h^{-3/2}$ and $0.077h^{-3/2}$ in the two groups, considerably higher than values reported in the literature for other groups within smaller radii. Extrapolated gas mass fractions at r_{200} of $0.077h^{-3/2}$ and $0.089h^{-3/2}$ are slightly lower, but comparable to, values found for more massive clusters. These results emphasize the importance of extending group studies to large radii, in order to obtain reliable information on the amount and distribution of baryonic and dark matter in these systems.

- The radial variation of gas entropy in the two groups shows no evidence for a large isentropic core, at variance with predictions from simple preheating scenarios. The poorly resolved temperature profiles prohibit any firm conclusions on the entropy behaviour at large radii, but evidence for excess entropy with respect to that expected from self-similar scaling of observed massive clusters is seen out to at least r_{500} . Such a large-radius excess would be consistent with the predictions of some simulations including heat sources, and with smooth accretion theory. As an alternative for the origin of excess entropy at all scales, radiative cooling alone is ruled out by the relatively high gas mass fractions derived for these systems.

ACKNOWLEDGMENTS

We thank Andy Read and Ben Maughan for many useful discussions and use of their X-ray analysis scripts, Laurence Jones for discussions of the WARPS data, and Gary Wegner (Dartmouth College) and Harald Ebeling (Univ. of Hawaii) for letting us use these data prior to publication. Tadayuki Kodama is thanked for providing us with his elliptical galaxy evolution models. This work acknowledges the use of the Starlink facilities at Birmingham, the Lyon and NASA Extragalactic Databases, and the ROSAT All-Sky Survey and 2-Micron All-Sky Survey databases. JR acknowledges support by the Danish Natural Science Research Council (SNF).

REFERENCES

- Anders E., Grevesse N., 1989, *Geochim. Cosmochim. Acta* 53, 197
- Arnaud M., Evrard A.E., 1999, *MNRAS*, 305, 631
- Ascasibar Y., Yepes G., Müller V., Gottlöber S., 2003, *MNRAS*, submitted (astro-ph/0306264)

- Babul A., Balogh M.L., Lewis G.F., Poole G.B., 2002, MNRAS, 330, 329
- Borgani S., Governato F., Wadsley J., Menci N., Tozzi P., Lake G., 2001, ApJ, 559, L71
- Borgani S., Governato F., Wadsley J., Menci N., Tozzi P., Quinn T., Stadel J., Lake G., 2002, MNRAS, 336, 409
- Cash W., 1979, ApJ, 315, 939
- Castillo-Morales A., Schindler S., 2003, A&A, 403, 433
- Davé R., Katz N., Weinberg, D.H., 2002, ApJ, 579, 23
- David L.P., Jones C., Forman W., 1995, ApJ, 445, 578
- Eke V.R., Navarro J.F., Frenk C.S., 1998, ApJ, 503, 569
- Ettori S., Fabian A.C., 1999, MNRAS, 305, 834
- Ettori S., De Grandi S., Molendi S., 2002, A&A 391, 841
- Evrard A.E., Metzler C.A., Navarro J.F., 1996, ApJ, 469, 494
- Fairley B.W., Jones L.R., Scharf C., Ebeling H., Perlman E., Horner D., Wegner G., Malkan M., 2000, MNRAS, 315, 669
- Frenk C.S., et al., 1999, ApJ, 525, 554
- Fukugita M., Hogan C.J., Peebles P.J.E., 1998, ApJ, 503, 518
- Grego L., Carlstrom J.E., Reese E.D., Holder G.P., Holzappel W.L., Joy M.K., Mohr J.J., Patel S., 2001, ApJ, 552, 2
- Helsdon S.F., Ponman T.J., 2000, MNRAS, 315, 356
- Jones C., Forman W., 1984, ApJ, 276, 38
- Jones L.R., Scharf C., Ebeling H., Perlman E., Wegner G., Malkan M., Horner D., 1998, ApJ, 495, 100
- Kodama T., Arimoto N., 1997, A&A, 320, 41
- Lewis G.F., Babul A., Katz N., Quinn T., Hernquist L., Weinberg, D.H., 2000, ApJ, 536, 623
- Loken C., Norman M.L., Nelson E., Burns J., Bryan G.L., Motl P., 2002, ApJ, 579, 571
- Lumb D.H., 2002, in Jansen F., ed., Proc. Symp., New Visions of the X-ray Universe in the XMM-Newton and Chandra Era, ESA SP-488 (astro-ph/0203277)
- Markevitch M., Forman W.R., Sarazin C.L., Vikhlinin A., 1998, ApJ, 503, 77
- Markevitch M., Vikhlinin A., Forman W.R., Sarazin C.L., 1999, ApJ, 545, 527
- Mason K.O., et al., 2000, MNRAS, 311, 456
- Miralda-Escude J., Babul A., 1995, ApJ, 449, 18
- Mohr J.J., Evrard A.E., Fabricant D.G., Geller M.J., 1995, ApJ, 447, 8
- Mohr J.J., Mathiesen B., Evrard A.E., 1999, ApJ, 517, 627
- Moore B., Governato F., Quinn T., Stadel J., Lake G., 1998, ApJ, 499, L5
- Mulchaey J.S., Zabludoff A.I., 1998, ApJ, 496, 73
- Mullis C.R., et al., 2003, ApJ, 594, 154
- Mushotzky R., Figueroa-Feliciano E., Loewenstein M., Snowden S.L., 2003, astro-ph/0302267
- Navarro J.F., Frenk C.S., White S.D.M., 1995, MNRAS, 275, 720
- Pedersen K., Yoshii Y., Sommer-Larsen J., 1997, ApJ, 485, L17
- Poggianti B.M., 1997, A&AS, 122, 399
- Ponman T.J., Cannon D.B., Navarro J.F., 1999, Nature, 397, 135
- Ponman T.J., Sanderson A.J.R., Finoguenov A., 2003, MNRAS, 343, 331
- Pratt G.W., Arnaud M., 2002, A&A, 394, 375
- Pratt G.W., Arnaud M., 2003, A&A, 408, 1
- Pratt G.W., Arnaud M., Aghanim N., 2001, in Neumann D.M., Tranh Thanh Van J., eds, Proc. Symp., Galaxy Clusters and the High Redshift Universe Observed in X-rays, astro-ph/0105431
- Read A.M., Ponman T.J., 2003, A&A, 409, 395
- Sanderson A.J.R., Ponman T.J., Finoguenov A., Lloyd-Davies E.J., Markevitch M., 2003, MNRAS, 340, 989
- Sarazin C.L., Wise M.W., Markevitch M.L., 1998, ApJ, 498, 606
- Scharf C.A., Jones L.R., Ebeling H., Perlman E., Malkan M., Wegner G., 1997, ApJ, 477, 79
- Schlegel D.J., Finkbeiner D.P., Davis M., 1998, ApJ, 500, 525
- Stark A.A., Gammie C.F., Wilson R.W., Bally J., Linke R.A., Heiles C., Hurwitz M., 1992, ApJS, 79, 77
- Sutherland R.S., Dopita M.A., 1993, ApJS, 88, 253
- Tozzi P., Norman C., 2001, ApJ, 546, 63
- Tully R.B., 1987, ApJ, 321, 280
- Vikhlinin A., McNamara B.R., Forman W., Jones C., Quintana H., Hornstrup A., 1998, ApJ, 502, 558
- Voit G.M., Balogh M.L., Bower R.G., Lacey C.L., Bryan G.L., 2003, ApJ, 593, 272
- Voit G.M., Ponman T.J., 2003, ApJ, 594, L75
- Xue Y.-J., Wu X.-P., 2000, ApJ, 538, 65